Corrosion Science 224 (2023) 111565

Contents lists available at ScienceDirect

Corrosion Science

journal homepage: www.elsevier.com/locate/corsci

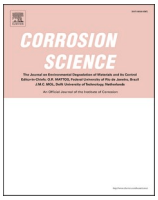

Low-temperature hot corrosion of arc evaporated $Ti_{1-x}Al_xN$ on Ni-Cr-Co based superalloys

O.E. Hudak [a,*], A. Scheiber [a], P. Kutrowatz [a], T. Wojcik [a], L. Shang [b], O. Hunold [b], S. Kolozsvári [c], P. Polcik [c], H. Riedl [a,d]

[a] Christian Doppler Laboratory for Surface Engineering of high-performance Components, TU Wien, Austria
[b] Oerlikon Balzers, Oerlikon Surface Solutions AG, 9496 Balzers, Liechtenstein
[c] Plansee Composite Materials GmbH, D-86983 Lechbruck am See, Germany
[d] Institute of Materials Science and Technology, TU Wien, A-1060 Wien, Austria

ARTICLE INFO

Keywords:
Low temperature hot corrosion
PVD coatings
Arc-evaporation
Superalloy

ABSTRACT

Cathodic arc evaporated $Ti_{1-x}Al_xN$ coatings were deposited on a Nimonic c-263 superalloy and tested under low temperature hot corrosion conditions. Treated with a $MgSO_4/Na_2SO_4$ salt-mixture, all samples were annealed at 700 °C in a 2800 $ppm_{(volume)}$ SO_x-rich atmosphere for 1, 5, 15 and 30 h. A significantly reduced corrosion severity was exhibited by all $Ti_{1-x}Al_xN$ variants over the uncoated NiCrCo alloy. A synergistic fluxing mechanism was found to be the dominant factor for the coating breakdown. Depending on the relative Al-to-Ti content on the $Ti_{1-x}Al_xN$ sublattice, differences in the coatings' corrosion and scaling behavior were observed.

1. Introduction

Superalloys are well known for their excellent mechanical strength, creep-profiles and fatigue properties at high-temperatures, as well as good corrosion and oxidation resistance in highly demanding environments [1–4]. Finding wide application in industrial gas turbines (IGT) and jet engines, superalloys represent an indispensable material class in energy generation sectors and modern aviation [1,5–8]. However, superalloys are also known for their susceptibility to molten salt-induced corrosion – better known as hot corrosion (HC) [5,9–12].

For this reason, protective coatings provide a lucrative solution in combatting HC-attack of turbine elements [13]. Many coating systems have shown improved oxidation and corrosion resistance in high temperature settings, such as metallic NiCrAlY coatings [14–16], metallic gradient coatings [17], ceramic oxide coatings [18], nitride coatings [19–22], silicides [23–25], and enamel [26,27], but remain far from being optimal. The variety of these studies not only demonstrates the complexity of hot corrosion phenomena, but also confirms that there is a need for a more refined understanding of the corrosion mechanisms in thin films.

With focus on industrially established Ni-Cr-Co- base superalloys, the objective of this study is to provide a detailed analysis of the hot corrosion behavior of protective physical vapor deposited $Ti_{1-x}Al_xN$ coatings. Cathodic arc evaporated (CAE) $Ti_{1-x}Al_xN$ depicts one of the most established coating system in diverse industrial sectors, based on its unique combination of thermo-mechanical properties. However, the use in HC environments is relatively unexplored and detailed understanding of ongoing mechanisms are rare.

1.1. Hot corrosion in gas turbines

When salt-rich aerosols from marine environments enter the combustion chamber through the air intake (e.g. NaCl, $MgCl_2$, etc.), they react with oxygen and sulfur baring combustion gases and form high-melting sulfate salts (e.g. Na_2SO_4 and $MgSO_4$) [28–31] (Eqs. 1–4). When exiting the combustion chamber, these highly stable salts can build up on hot sections of the gas-turbines, where they adhere and cause severe degradation of the material surfaces. Especially components, which come in direct contact with the combustion gases, such as transition lines from the combustion chamber, as well as blades and vanes of the high-pressure turbine (HPT) and low-pressure turbine (LPT) are vulnerable to hot gas corrosion.

$$S + O_2 \rightarrow SO_2 \quad (1)$$

$$SO_2 + 1/2O_2 + \frac{(M)}{catalyst} \leftrightarrow SO_3 \quad (2)$$

* Corresponding author.
E-mail address: oliver.hudak@tuwien.ac.at (O.E. Hudak).

https://doi.org/10.1016/j.corsci.2023.111565
Received 10 July 2023; Received in revised form 19 September 2023; Accepted 28 September 2023
Available online 29 September 2023

$$2NaCl + S + 2O_2 \rightarrow \alpha - Na_2SO_4 + Cl_2 \; T_{m(Na_2SO_4)} = 884^{\circ}C \quad (3)$$

$$MgCl_2 + S + 2O_2 \rightarrow MgSO_4 + Cl_2 \; T_{m(MgSO_4)} = 1124^{\circ}C \quad (4)$$

Depending on the physical aggregate of these salt-deposits, one of two corrosion mechanisms can ensue: Low temperature hot-corrosion (LTHC, 575–800 °C), where the salt adheres in a solid form, or high temperature hot corrosion (HTHC, 800–950 °C), where the deposit exits in a molten state.

The corrosion of alloys and coatings by hot gas corrosion then proceeds in several key steps: An incubation stage, an initiation stage, a propagation stage, followed by failure [32,33] The incubation stage features the formation of stable oxide scales (e.g. TiO_2, Al_2O_3, NiO, and Cr_2O_3), whereby a steady state (passivity) against further oxidation is provided. The incubation state is especially interesting when considering coated superalloys, as the oxides that form on the coating surface typically differ from those of the bulk material.

The subsequent initiation stage comprises a sequence of changes in the materials environment that establishes the conditions where accelerated corrosion/degradation occurs. During this stage several processes take place, such as the deposition of a salt-film, the melting of the salt deposit (HTHC), and/or the formation of low-melting eutectics between the salt-deposit and metal oxide surface (LTHC). Furthermore, changes in the melt-basicity, and local depassivation of the oxide scale allows for accelerated attack of the underlying alloy/metal.

The initiation is then followed by the propagation, where an accelerated progression of both, depassivation of the protective metal oxide scale, and internal sulfidation and oxidation of the now unprotected bulk material occurs.

Lastly, after a given duration, the corrosion front has infiltrated the material to such extend, that the integrity of the component fails.

1.2. Depassivation via fluxing mechanisms

When protective oxides such as Al_2O_3, TiO_2, NiO or Cr_2O_3 come in contact with fused Na_2SO_4, their dissolution can occur in one of two ways: Basic dissolution (basic fluxing), where the oxide reacts with the basic component (Na_2O) of the melt, or acidic dissolution (acidic fluxing), where the oxide reacts with the acidic component of the melt (SO_3) (Eq. 5).

$$Na_2SO_{4(l)} \leftrightarrow Na_2O_{(diss.(basic))} + SO_{3(g,(acidic))} \quad (5)$$

In a series of electrochemical studies, Zheng [34], Rapp and Luthra [35] investigated the solubility of various oxides in fused Na_2SO_4 at 1200 K. By varying the basicity of the melt, the solubility of most oxides (with the exception of SiO_2) features distinct solubility minima. Fig. 1a shows a compilation of such measured solubilities, by plotting the concentration of the dissolved oxide over the basicity of the melt.

Which reaction dominates (acidic dissolution or basic dissolution) depends on the chemical stability of the oxide (position of the solubility minimum). While Al_2O_3 and Cr_2O_3 are considered acidic oxides (stable in acidic conditions), Co_2O_3 and NiO are viewed as basic oxides (stable in more basic conditions). Therefore, Co_2O_3 and NiO are predominantly dissolved via an acidic fluxing mechanism (reacts with SO_3), while Al_2O_3 and Cr_2O_3 are readily dissolved in more neutral and basic melts (basic fluxing by reacting with Na_2O).

However, when different oxides are situated in close proximity to one another and stand in contact with a fused salt deposit, a superimposed mechanism can take place, referred to as synergistic fluxing. This is particularly dangerous for alloys and coatings which rely on a mixed and/or layered oxide scale, in order to combat hot corrosion. If the salt basicity of the melt falls between the solubility minima of such two oxides, the solubility of the one oxide can facilitate melt conditions that accelerates the dissolution of the other (Fig. 1b).

As the oxidation of $Ti_{1-x}Al_xN$ coatings is dominated by the formation of Al_2O_3 and TiO_2, a central point of discussion throughout this study are

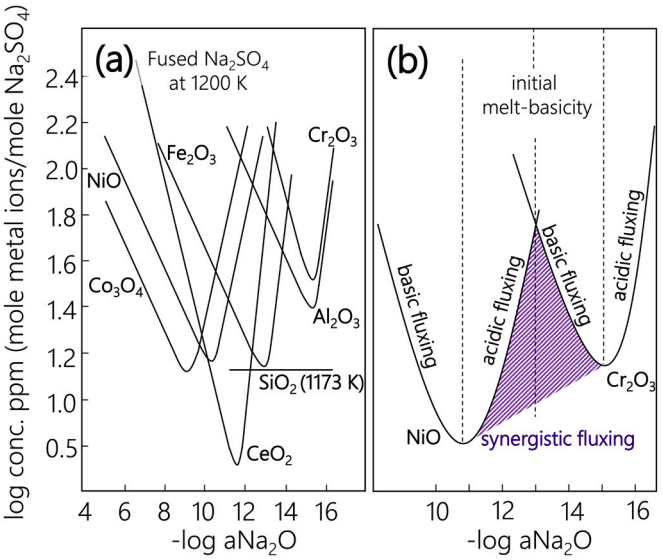

Fig. 1. (a) Solubility diagram of common oxides in fused Na_2SO_4 as a function of melt-basicity (reworked from [36]), (b) region of synergistic fluxing between NiO and Cr_2O_3 (shaded area).

synergistic effects in the fluxing mechanism. Thus, the authors intend to provide a fundamental understanding of the respective LTHC mechanisms for arc-evaporated $Ti_{1-x}Al_xN$ coatings, by showcasing how different Al to Ti contents influence the corrosion behavior.

2. Experimental

2.1. Coating depositions

All $Ti_{1-x}Al_xN$ coatings were deposited using an industrial scale cathodic arc-evaporation system (Innova 1.0, Oerlikon Surface Solutions AG). 10 µm thick $Ti_{1-x}Al_xN$ coatings with varied Al contents ($Ti_{0.52}Al_{0.48}N$ and $Ti_{0.34}Al_{0.66}N$) were deposited using TiAl (50/50 at%) and TiAl(34/66 at%) targets, respectively (Plansee Composite Materials GmbH). The coatings were grown in a pure N_2 atmosphere at a pressure of 3.5 Pa and a deposition temperature of 450 °C. Furthermore, a target current of 200 A and a bias potential up to − 40 V were chosen for all depositions.

Single-crystalline Si stripes (100-oriented, 20×7x 0.38 mm) and Nimonic c-263 (VDM-Metals, Germany) were used as substrate materials. Whereas coated Si-substrates were solely used for coating-characterization purposes (e.g. analysis of the coatings morphology via fracture cross-section, and coating thickness measurements), the coated Nimonic c-263 alloys (detailed chemical composition, see Table 1) were exclusively used for hot corrosion experiments and post-corrosion analysis.

Prior to the depositions, all substrates were ultrasonically cleaned with acetone and ethanol before mounting them onto the carousel of the deposition chamber. With a base pressure of $< 5.0^{-4}$ Pa, the substrates were further cleaned for 25 min by a central-beam argon plasma etching procedure (Oerlikon Surface Solutions AG).

2.2. Corrosion experiments

The hot gas corrosion testing-rig was conceptualized in three sections: (i) the gas-mixing system (inlet), (ii) a reaction module, and (iii) a gas-treatment system (outlet). For the composition of the experiment's atmosphere, a combination of three gas-inlet feeds were controlled via mass-flow controllers. A total gas-flow (total pressure, p) of 2500 sccm was chosen, comprised of 2118 sccm [Ar], 375 sccm [O], and 7 sccm [SO_2]. This translates to partial pressures of $p_{[Ar]} = 8.47 \times 10^{-1}$ atm,

Table 1
Nominal chemical composition (wt%) of the Nimonic c-263 superalloy.

	Ni	Co	Cr	Mo	Ti	Al	Fe	Si
Nimonic c-263 [4]	47–54	19–21	19–21	5.6–6.1	1.9–2.4	0.3–0.6	0–0.7	0–0.4

$p_{[O]} = 1.5 \times 10^{-1}$ atm and $p_{[SO2]} = 2.8 \times 10^{-3}$ atm, respectively. The mixed gases then enter the reaction chamber, positioned inside a three-zone gradient oven (Carbolite Gero GmbH & Co. KG). A quartz-tube flow-reactor safely accommodates the aggressive SO_x-rich atmosphere in liaison with the high temperatures (700 °C) needed for the HC experiments. Lastly, the exhaust gases are washed in a NaOH bath before exiting the set-up. A detailed illustration of the HC-testing rig is provided in Appendix Figure A1.

For every corrosion experiment, two sets of sample-arrangements were considered: (i) a control-arrangement, were no salt was added to the sample surfaces, and (ii) an experimental-arrangement, where samples were prepped with salt-coupons to mimic hot-corrosion conditions.

A mixture of anhydrous $MgSO_4$ and Na_2SO_4 (Merck KGaA) with a molar ratio of 20:80, or mass ratio of 15.21:84.78, respectively, was chosen for all experiments. A saturated aqueous solution was then prepared. Using a pipette, small droplets were applied onto the sample surfaces and dried under ambient conditions for several days.

With reference to the calculated binary-phase diagram from Yazhenskikh et. al., a solidus temperature of ~725 °C and a liquidus temperature of ~810 °C were estimated for the salt-coupons, which was later confirmed in a series of annealing experiments [31]. In order to remain below the liquidus temperature of the salt-mixture (prerequisite for LTHC is a solid aggregate state), a temperature of 700 °C was chosen for all corrosion experiments.

After loading the quartz tube with the control-arrangement and the salt-loaded samples, the chamber was sealed and purged for 10 min with 2000 sccm Ar. Subsequently, the furnace was turned on whilst continuing purging with Ar. With a ramp-rate of 20 °C/min, 45 min were allocated for reaching the desired 700 °C, after which an additional 15 min were allotted for ensuring a homogeneous temperature distribution within the quartz-tube. Following the heat-up sequence, the Ar, O_2, and SO_2 mass-flow controllers were set to 2118 sccm, 375 sccm and 7 sccm (2800 ppm SO_2 by volume), respectively, and their hand valves opened, marking the beginning ($t_{0\,h}$) of the corrosion experiment. After the desired duration of the experiment has elapsed (e.g. t = 1, 5, 15, and 30 h), the furnace was turned off, the hand-valves for the O_2 and SO_2 feeds closed, and the chamber purged with 2000 sccm Ar until the temperature within the quartz-tube was < 200 °C.

2.3. Analytical methods

For studying the morphological properties, such as coating thickness and the integrity of the substrate-coating interfaces, a Zeiss Sigma 500 VP high-resolution field emission gun scanning electron microscope (FEGSEM) was used. With an acceleration voltage, ranging between 3 kV and 6 kV, characterization of coating thickness and morphology were performed on fracture cross sections of coated Si-substrates. Furthermore, the FEGSEM, combined with an EDAX Octane elect system for energy dispersive X-ray spectroscopy (EDX), was used for quantitative chemical investigations.

For crystallographic analysis, Bragg-Brentano X-ray diffraction (BBHD) was utilized, using a PANalytical XPert Pro MPD system equipped with a Cu-Kα radiation source (wave length λ = 1.54 Å).

For post corrosion characterization, top-view images were taken, using a digital light microscope. For salt loaded samples, the deposit was carefully removed and any remnant salt washed off with distilled water, in order to expose the oxidized coating surfaces. Subsequently, anew XRD measurements were conducted, after which the samples were embedded in a conductive polymer-matrix, their cross-sections thoroughly grinded, polished, and analyzed using a Zeiss Sigma 500 VP high-resolution FEGSEM. EDX line-scans, as well as EDX-mapping, were utilized for identifying diffusion pathways, phase-transformations, and coating breakdown.

Lastly, transmission electron microscopy (TEM), FEI TECNAI F20, equipped with a field emission gun and operated at an accelerating voltage of 200 kV) was conducted. Bright-field (BF) imaging was utilized to learn more about the microstructure, diffusion processes and the overall corrosion mechanism. For the preparation for the TEM lamella a standardized focused-ion beam (FIB) lift-out technique was used (Scios 2 DualBeam system, ThermoFisher Scientific).

3. Results

3.1. Structure and morphology

The as-deposited fracture cross-sections of both, low-Al content $Ti_{0.52}Al_{0.48}N$ and high Al-content $Ti_{0.34}Al_{0.66}N$ coatings are shown in Figs. 2a and 2b, respectively. With a thickness of 9.8 µm ($Ti_{0.52}Al_{0.48}N$) and 10.1 µm ($Ti_{0.34}Al_{0.66}N$) both coating variants feature a homogeneous and dense columnar microstructure. The chemical compositions normalized to the metallic sublattice, $Ti_{0.52}Al_{0.48}N$ and $Ti_{0.34}Al_{0.66}N$, were determined by EDX and deviate only slightly from their target compositions (50/50 and 35/65 at%, respectively). Structural analysis by XRD indicate a dominant cubic-Ti(Al)N crystal structure for both coating variants, with only slight indications of the thermodynamically

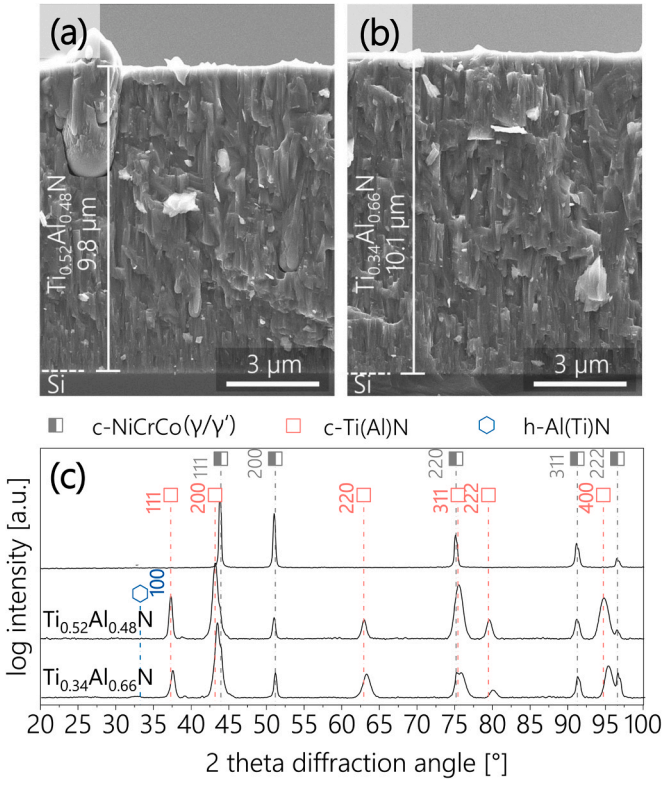

Fig. 2. Characterization of as-deposited $Ti_{1-x}Al_xN$ coatings: (a-b) show the fracture cross-sections of the $Ti_{0.52}Al_{0.48}N$ and $Ti_{0.34}Al_{0.66}N$ on Si, respectively, whereas (c) features XRD spectra of the $Ti_{1-x}Al_xN$ coatings and NiCrCo substrate material. Reference patterns were taken from ref. [37–39].

favored wurzite-Al(Ti)N phase visible for the high Al-content $Ti_{0.34}Al_{0.66}N$ coating see Fig. 2c.

3.2. Low temperature hot corrosion experiments

Fig. 3 features top-view images of all samples that have been subject to the hot-corrosion experiments. At 700 °C and a partial pressure of $p_{[SO2]} = 2.8 \times 10^{-3}$ atm (2800 ppm by volume), all samples were exposed to the same corrosive atmosphere and annealed for 1, 5, 15 and 30 h. Shown on the left is the so-called control group (samples without salt deposit), consisting of the uncoated NiCrCo-alloy, the $Ti_{0.52}Al_{0.48}N$ and $Ti_{0.34}Al_{0.66}N$ coated samples, listed from top to bottom. For each sample, gradual changes in the interference colors are observed that relate to evolving oxide scales. Particularly for the initially polished NiCrCo substrate, the evolution of the typical brownish NiO-scaling after 30 h is quite apparent.

On the right-hand side, the surfaces of the salt-loaded samples are shown before (0 h) and after the corrosion experiments (1–30 h). Significant corrosion can be observed for the uncoated NiCrCo-alloy. After 1 h, dark brown corrosion products appear at the border of the salt-deposit. As the duration of the corrosion experiment is prolonged, the corrosion front expands radially, whilst consuming the salt deposit (5 h). After 15 h, the entire alloy surface is covered with porous corrosion products, while the consumption of the salt deposit continues. After 30 h, all the salt has been taken up, leaving a completely deteriorated alloy-surface behind.

Contrarily, the corrosion progression and uptake of the salt-deposit for the $Ti_{1-x}Al_xN$ coated samples occurs much more delayed. After 1 h, no visible corrosion products form at the salt-deposit borders. After 5 h, an onset of surface degradation can be seen, which remains unchanged throughout 15 h. Only at 30 h, significant deterioration of the coating structure, as well as salt uptake is featured. We believe that the substantial consumption of the salt observed for the $Ti_{0.52}Al_{0.48}N$ is a sign for a breakthrough of the coating structure, where the salt has breached the protective coating and is able to react with the NiCrCo-substrate underneath.

3.3. Oxidation behavior without salt deposits

The oxidation behavior and scale formation of $Ti_{1-x}Al_xN$ coatings is well documented in literature, reporting the formation of a thin but continuous oxide scale in air at temperatures as low as 700–750 C [40, 41] However, depending on the coating's Al content and annealing temperature, distinct differences in the scale growth were observed. While coatings with lower Al-contents, such as $Ti_{0.75}Al_{0.25}N$ and $Ti_{0.56}Al_{0.44}N$ preferentially develop a double-layered oxide (so called type 1 oxidation, featuring an Al-rich upper layer and a Ti-rich sublayer), higher Al-content coatings like $Ti_{0.34}Al_{0.66}N$ tend to generate a mixed oxide scale (type 2 oxidation), with no separation between the Ti- and Al-diffusion profiles [41,42]. Coatings with Al concentrations falling between type 1 and type 2 follow a T-type oxidation behavior. Similar to type 1, the T-type oxidation exhibits a layered oxide, however, with less separation between the individual Al- and Ti-diffusion gradients.

By annealing $Ti_{0.52}Al_{0.48}N$ and $Ti_{0.34}Al_{0.66}N$ coatings in a 2800 ppm SO_x-rich atmosphere at 700 °C (control group), this behavior was only partially observed. While both coatings do feature the formation of Al_2O_3 and TiO_2 oxide scales, their scale structure appears quite similar and seem to follow a T-type oxidation (layered structure with an Al-rich upper layer, and a Ti-rich sublayer).

Figs. 4a and 4b, show EDX line scans obtained from the annealed $Ti_{0.52}Al_{0.48}N$ and $Ti_{0.34}Al_{0.66}N$ coatings, respectively, and intend to highlight the relative distribution of Al and Ti after 1, 5, 15, and 30 h at the coating surfaces. Apparent are layered diffusion profiles, where an Al-rich band forms on top and a Ti-rich zone underneath. As neither of the coatings demonstrates complete Al diffusion to the surface (substantial Al-content >10 at% remains within the Ti-rich sublayer), both coating fall within the type T oxidation regime. This only partially agrees with the model from Greczynski et al., which predicts a type 2 oxidation behavior for the higher Al-content $Ti_{0.34}Al_{0.66}N$ samples at 700 °C. At this point, the authors would like to point out that EDX may

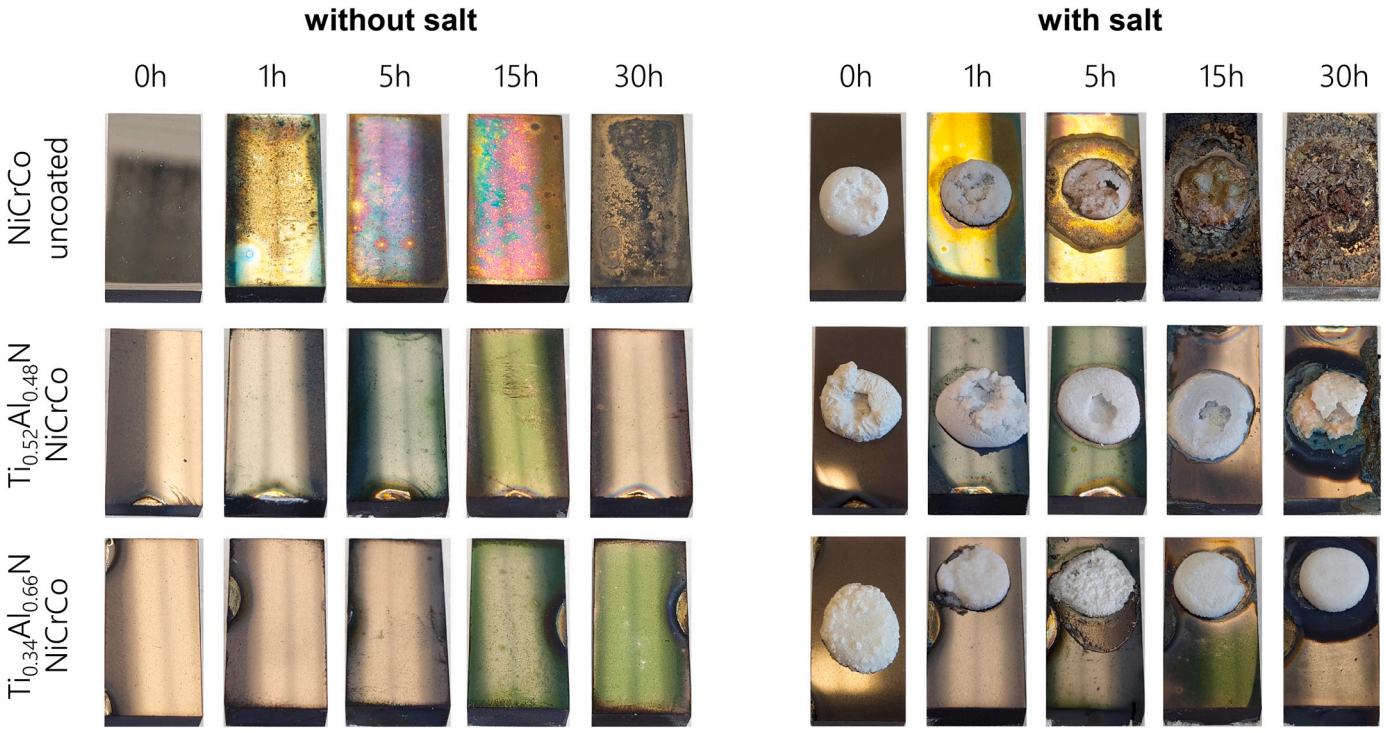

Fig. 3. Top-view images showing annealed samples at 700 °C in SO_x-rich atmosphere without salt-deposits for 0, 1 h, 5 h, 15 h and 30 h (left group), as well as annealed samples with salt-deposits under identical conditions (right group). The first row features uncoated Nimonic c-263 substrates, while the second and third row show $Ti_{0.52}Al_{0.48}N$ and $Ti_{0.34}Al_{0.66}N$ coated c-263 substrates, respectively.

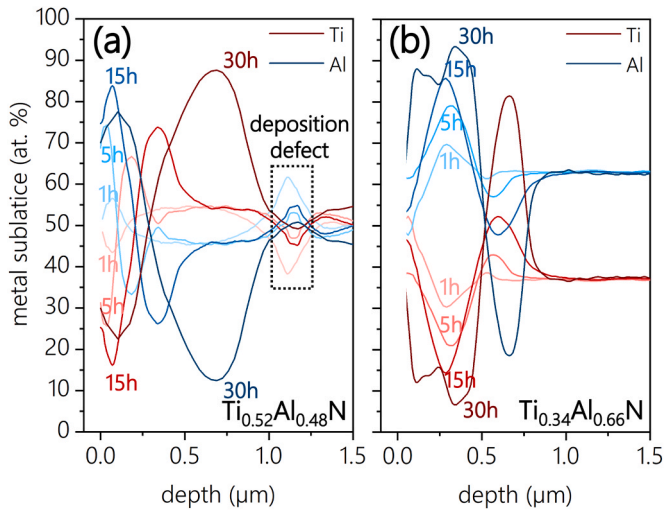

Fig. 4. EDX line scans for the annealed (a) $Ti_{0.52}Al_{0.48}N$ and (b) $Ti_{0.34}Al_{0.66}N$, highlighting the Al- and Ti-diffusion profiles of the metal sublattice after 1, 5, 15, and 30 h.

not be the most accurate analytical choice for making this observation and urge to treat this discrepancy with caution, particularly as the Al-chemistry $Ti_{0.34}Al_{0.66}N$ sits right at the border of the type-T and type-2 regimes.

As for the relative thicknesses of the Al- and Ti-rich layers, the $Ti_{0.52}Al_{0.48}N$ coatings feature a thinner Al-rich scale on top of a thicker Ti-dominated layer, whereas the $Ti_{0.34}Al_{0.66}N$ coatings develop a thicker Al-rich scale on top of a thinner Ti-band. This again stands in good agreement with observations made by Greczynski et al. [42], and Panjan et. al. [41], who reported that coatings with increasing AlN concentrations produce thinner overall oxides, but with a thicker Al-rich top layer.

Figs. 5a and 5b presents the structural evolution of $Ti_{0.52}Al_{0.48}N$ and $Ti_{0.34}Al_{0.66}N$ coatings without salt deposits annealed at 700 °C (1, 5, 15, and 30 h) in a 2800 ppm SO_x-rich atmosphere. Interestingly, indications of the rutile-TiO_2 structure are observed for both coatings in their as deposited state, which can be explained by a post-deposition venting strategy that facilitates oxygen to the not yet fully cooled coating surfaces [43]. As the coatings are annealed at 700 °C for 1 h, transformation of the metastable c-Ti(Al)N phase into the thermodynamically more favorable w-Al(Ti)N phase occurs for both compositions. While the $Ti_{0.52}Al_{0.48}N$ coating features intensified reflexes of the [002]-planes, the $Ti_{0.34}Al_{0.66}N$ coating exhibits more pronounced diffraction along the [100]-direction.

With increasing annealing time (5–15 h), the formation of additional oxides, such as α-Al_2O_3 and TiO_2 (anatase) occurs. For $Ti_{0.52}Al_{0.48}N$, reflexes of the α-Al_2O_3 and TiO_2 (anatase) are most pronounced in the [012]- and [101]-direction, respectively, while for the $Ti_{0.52}Al_{0.48}N$ coating, preferred diffraction of the same oxides occurs along the [202]- and [103]-planes.

Hereafter, no additional oxides develop, apart from the already mentioned TiO_2 (rutile), TiO_2 (anatase), and α-Al_2O_3. Interestingly, no sulphation of the surface oxides occurs for the duration of the annealing experiments despite the oxide to sulphate transformation being thermodynamically favored. This is a strong indication that an insufficiently high partial pressure of SO_3 is present [44]. By consulting the global kinetic model by Burdett et al. [45], together with studies from Wall et. al [29] and Anthony et. al. [46], an approximation of the homogeneous SO_3/SO_2 conversion rate was made, rendering a partial pressure of $p_{[SO3]}$ ~2.0×10^{-3} atm (or ~200 ppm by volume).

3.4. Oxidation behavior of salt-loaded samples

Compared to the coatings, which have been annealed solely in a SO_x-rich atmosphere (Fig. 5a & 5b), a significantly higher oxidation rate was observed for coatings that were loaded with salt deposits under identical annealing conditions (Fig. 6a & 6b). In order to retrieve information about the oxidized state of the coatings, the salt deposits were carefully removed from the samples prior to the XRD measurements.

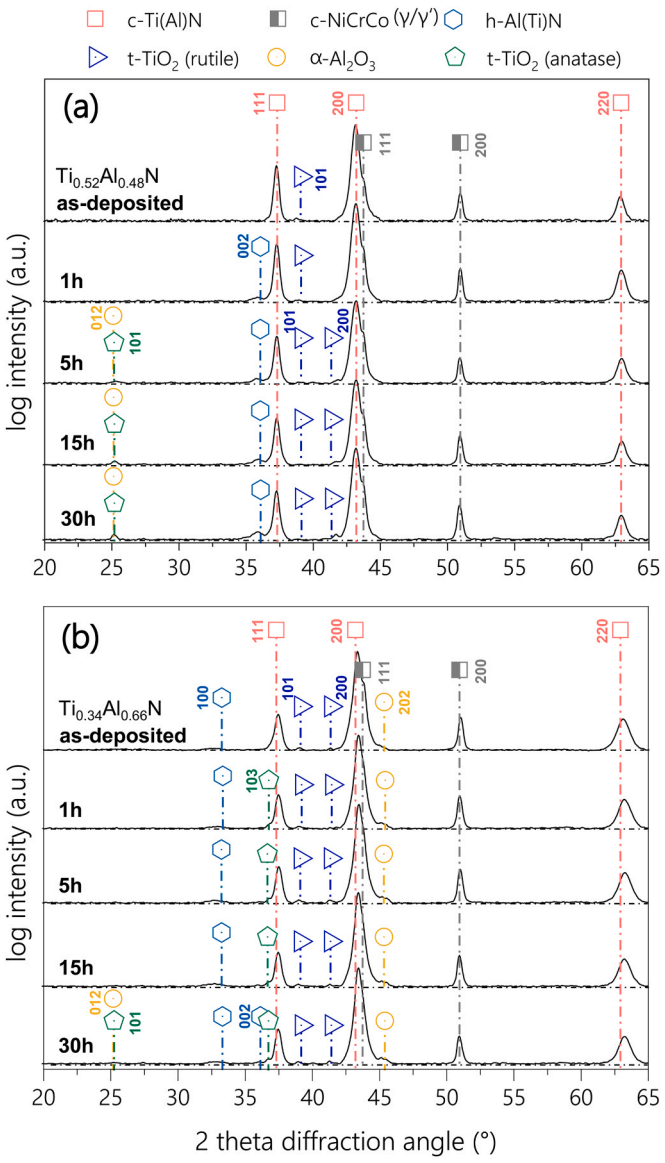

Fig. 5. XRD analysis of (a) $Ti_{0.52}Al_{0.48}N$ and (b) $Ti_{0.34}Al_{0.66}N$ coatings after annealing in SO_x-rich atmosphere at 700 °C for 0, 1, 5, 15, and 30 h (reference patterns were taken from ref. [37–39,47–49].

By reviewing the respective diffractograms, a more prominent onset of oxide formation between 1 and 5 h is readily apparent. Both $Ti_{0.52}Al_{0.48}N$ and $Ti_{0.34}Al_{0.66}N$ coatings (Fig. 6a-b) feature more distinct reflexes of the TiO_2-anatase [101]-planes and α-Al_2O_3 [012]-planes, as well as additional peaks referring to the TiO_2-rutile [110]-planes.

After 15 h, more pronounced diffraction peaks of the previously mentioned TiO_2-anatase and α-Al_2O_3 are exhibited for both compositions, while additional diffraction peaks of Cr_2O_3 appear in the diffractogram for $Ti_{0.52}Al_{0.48}N$. As chromium can only originate from the substrate, the detection of Cr_2O_3 indicates a breakthrough of the corrosion front into the substrate material. Other oxides such as Co_3O_4 and NiO, which would also readily form in the case of substrate oxidation, unfortunately, overlap with other prominent diffraction peaks, and thus, cannot be clearly interpreted. Contrarily, no Cr_2O_3 reflexes are

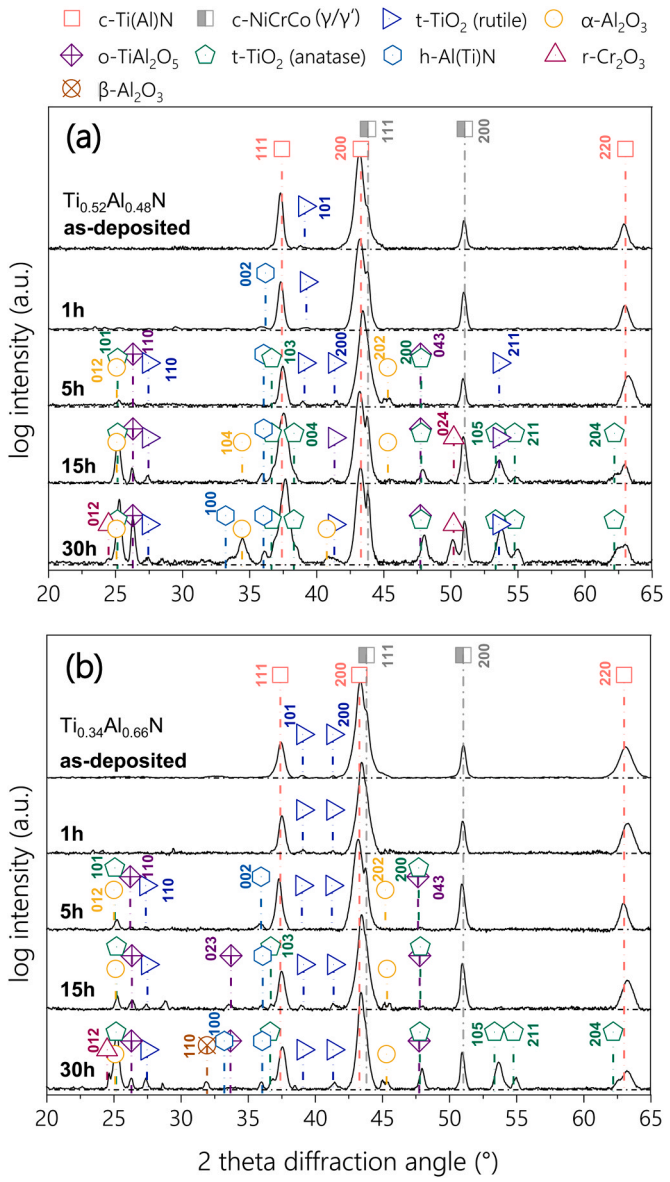

Fig. 6. XRD analysis of (a) $Ti_{0.52}Al_{0.48}N$ and (b) $Ti_{0.34}Al_{0.66}N$ coatings, which have been loaded with salt-deposits and annealed in an SO_x-rich atmosphere at 700 °C for 0, 1, 5, 15, and 30 h. Reference patterns were taken from ref. [37–39,47–51].

shown for the $Ti_{0.34}Al_{0.66}N$ coating after 15 h, suggesting that no breakthrough of the coating structure is present.

After 30 h of exposure to LTHC conditions, both coating variants feature severe oxidation and partial breakthrough of the corrosion front, validated by the structural evolution of rutile-TiO_2, α-Al_2O_3 and Cr_2O_3. Lastly, the formation of β-Al_2O_3 can be identified for the high Al-content $Ti_{0.34}Al_{0.66}N$ coating, which is a metastable structure that form in the presence of sodium aluminate ($NaAl_{11}O_{17}$).

3.5. Localized corrosion of $Ti_{1-x}Al_xN$ coatings under LTHC conditions

EDX line scans were collected along the cross-section of severely corroded coating sections. Fig. 7a & 7b show oxygen profiles, which serve as elemental indicators for the progression (depth) of the hot corrosion front. Since corrosion products that form during hot corrosion mostly comprise oxygen-containing compounds (oxides and sulfates), the diffusion depth of oxygen may provide first insights into the corrosion resistance of applied coating materials.

During the first 5 h of the corrosion experiments, the EDX profiles of both compositions display surface near oxygen enrichment, reaching diffusion depths of ~1 μm. After 15 h a significant increase in the oxygen diffusion rate is observed for the $Ti_{0.52}Al_{0.48}N$ coating variant, reaching a depth of ~8 μm. This is not the case for the higher Al-content $Ti_{0.34}Al_{0.66}N$ coating, which continues to exhibit a diffusion depth of only ~1 μm, however with a higher oxygen saturation than after 5 h.

Finally, after 30 h, accelerated oxygen diffusion is also observed for the high Al-containing $Ti_{0.34}Al_{0.66}N$ coating, with a diffusion depth of ~8 μm. As for the $Ti_{0.52}Al_{0.48}N$ coating, which already exhibited the accelerated diffusion behavior after 15 h, a complete bridging of the ~10 μm coating structure was measured, with the corrosion front reaching well into the underlying substrate material (>12 μm total diffusion).

Fig. 7c features a plot of the oxygen diffusion depths against the duration of the corrosion experiments, and highlights two stages: (i) an initiation stage, which involves surface-near oxygen enrichment and oxide scale development (~1 μm), and (ii) a propagation stage, which is characterized by accelerated oxygen inward diffusion. Apparent is that the higher Al-content $Ti_{0.34}Al_{0.66}N$ resides much longer within the initiation stage than the $Ti_{0.52}Al_{0.48}N$ coating (for 15 and 5 h, respectively), and consequently enters the propagation stage much later.

Unfortunately, LTHC is characterized by a pitting mechanism, which means that the corrosion progression of the coating occurs in a non-uniform (localized) manner. Therefore, the authors would like to emphasize that the oxygen profiles shown in Fig. 7a-c strictly pertain to the specific location they were obtained from and do not describe the overall state of the coating.

To further highlight this pitting behavior, Fig. 8 shows an EDX map of the salt-loaded $Ti_{0.52}Al_{0.48}N$ coating after 30 h, which has shown the highest oxygen inward diffusion (Fig. 7a) and exhibited Cr_2O_3 reflexes in the structural analysis as a clear indication for a corrosion front far beyond the coating ($Ti_{0.52}Al_{0.48}N$ loaded with salt after 30 h, Fig. 6a). Local corrosion pits emanate from regions where the coating structure has been breached, after which the corrosion front expands radially into the NiCrCo-base material. Also the corrosion of the coating itself occurs in homogeneously and is subject to local degradation. This is highlighted by the irregular diffusion profiles presented in Fig. 8 and can be summarized as follows:

i. Ti remains homogeneously distributed within the deposited coating.
ii. Al and N diffuse out of the coating structure and partially accumulate within the corrosion pit of the substrate.
iii. O diffuses into coating regions (lattice incorporation and/or atom replacement), where Al and N have defused outwards.
iv. O further diffuses into the NiCrCo-substrate material (radial pit-formation), where it reacts with Cr to form Cr_2O_3.
v. Ni and Co readily dissolve within the corrosion pit and diffuse outward.
vi. S accumulates at the corrosion front in the form of a highly concentrated S-band, however only within the pit of the substrate material.

3.6. Salt chemistry after LTHC experiments

Literature has shown that the LTHC mechanism hinges on the formation of a liquid salt/oxide interface [52]. The development of such a liquid interface, despite the corrosion temperature being well below the melting point of the salt-deposit, can occur in different ways. The so-called “gas phase induced acidic fluxing” is driven by high partial pressures of SO_3 in the atmosphere at relatively low temperatures (500–700 °C). First, sulphation of surface oxides that stand in direct contact with the atmosphere occurs, after which the development of low-melting eutectic mixtures between the newly formed sulphate scale and the salt-deposit follows (e.g. for Na_2SO_4 and $NiSO_4$ (mp= 680 °C) or

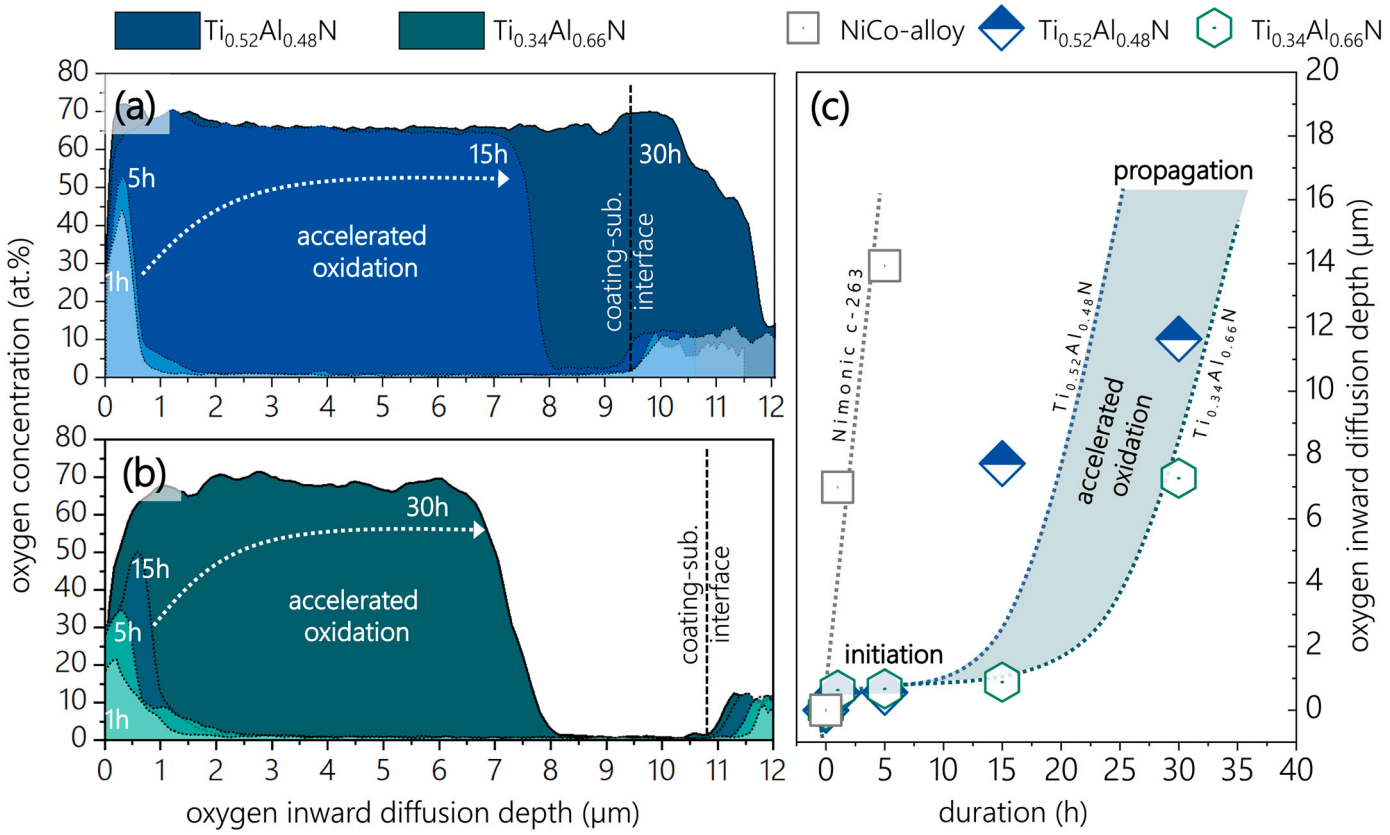

Fig. 7. EDX line-scan measurements of (a) the $Ti_{0.52}Al_{0.48}N$ and (b) the $Ti_{0.34}Al_{0.66}N$ coatings in their corroded states after 1, 5, 15, and 30 h. Depicted are the oxygen inward-diffusion profiles, which are indicative of the degree of oxidation that the coatings have suffered. (c) graphically highlights the prolonged oxidation resistance, due to the presence of the $Ti_{1-x}Al_xN$ coatings.

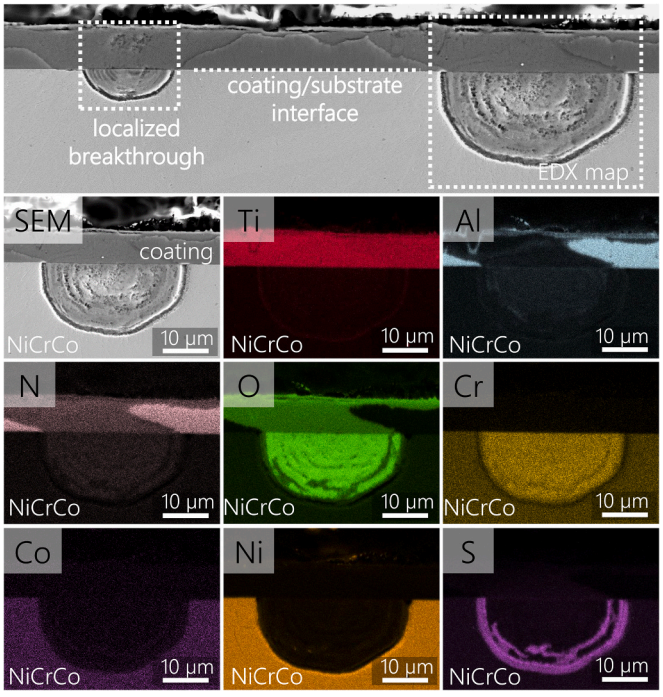

Fig. 8. Cross-section SEM imaging and EDX mapping showing localized breakthrough oxidation of the $Ti_{0.52}Al_{0.48}N$ coating, as well as the radial progression of the corrosion pit into the NiCrCo substrate material after 30 h of LTHC conditions.

Na_2SO_4 and $CoSO_4$ (mp= 575 °C) (see Eqs. 20–22). Other oxide-to-sulphate reactions are listed by Eqs. 23–25.

$$NiO_{(s)} + SO_{3(g)} = NiSO_{4(s)} \quad (20)$$

$$CoO_{(s)} + SO_{3(g)} = CoSO_{4(s)} \quad (21)$$

$$1/3Co_3O_{4(s)} + SO_{3(g)} = CoSO_{4(s)} + 1/6O_2 \quad (22)$$

$$Al_2O_{3(s)} + 3SO_{3(g)} = 1/2Al_2(SO_4)_3 \quad (23)$$

$$Fe_2O_{3(s)} + 3SO_{3(g)} = 1/2Fe_2(SO_4)_3 \quad (24)$$

$$Cr_2O_{3(s)} + 3SO_{3(g)} = 1/2Cr_2(SO_4)_3 \quad (25)$$

Another way is the "alloy induced acidic fluxing" referring to alloying elements, such as W, Mo, or V, that readily diffuse to the surface, oxidize, and react with Na_2SO_4 to form low-melting complex oxides that in turn induce acidic fluxing of the protective oxide scale of the alloy (see Eqs. 26–29) [52].

$$2SO_{2(g)} + O_{2(g)} = 2SO_{3(g)} \quad (26)$$

$$Mo + 3SO_{3(g)} = MoO_3 + 3SO_2 \quad (27)$$

$$MoO_{3(s)} + Na_2SO_{4(l)} = Na_2MoO_{4(diss.)} + SO_{3(g)} \quad (28)$$

$$MoO_{3(diss.in\ Na_2SO_4)} + Al_2O_{3(s)} = Al_2(MoO_4)_{3(diss.)} \quad (29)$$

In the case of a $Ti_{1-x}Al_xN$-coated NiCrCo-alloy, the latter alloy-induced fluxing mechanism may not be the most suitable model to explain the formation of a liquid salt/oxide interface, as a direct diffusion through the coating structure of such alloying elements has not

been detected and is highly unlikely. Instead, the authors propose a gas-phase induced process, where the SO_x/O_2-rich atmosphere diffuses to locations where the deposit adheres to the coating surface. Due to the porous nature of the salt deposits, diffusion of the SO_x/O_2-rich gas through the salt-structure is possible, allowing the atmosphere to come in contact with the coating surface. There, the formation of oxides (TiO_2 and Al_2O_3) takes place, after which sulphation of the developed oxides (see Eqs. 20–25) and subsequent formation of low-melting eutectic sulfate mixtures with the Na_2SO_4 deposit occurs.

During the formation of the liquid interface between the sulphate and sintered Na_2SO_4 deposit, a liquid junction forms that slowly acidifies through the uptake of the SO_3-rich gas. It is important to keep in mind, that low partial pressures of SO_3 are not enough for sulphating surface-oxides such as t-TiO_2 and h-Al_2O_3 at 700 °C, as proven by the control group (SO_3-rich atmosphere without Na_2SO_4 deposit– revisit Fig. 3). This implies that the salt-oxide interface is a necessary requisite for the oxide-sulphate transformation and essential for establishing conditions for the subsequent accelerated oxidation of the remaining coating structure. Without the acidification of the Na_2SO_4 deposit at the salt-coating interface, no stable sulphation is possible and no low-melting liquid film can be generated. Luthra [35] first demonstrated that the transport of possible ionic species through a liquid Na_2SO_4 film (e.g. $S_2O_7^{2-}$, SO_3^{2-}, and O^{2-}), and therefore its acidity, is dominated by the solubility of SO_3 as $S_2O_7^{2-}$ through exchange reactions with SO_4^{2-}. Luthra [35] also showed that gaseous species, such as O_2 and SO_2, have very low solubilities in Na_2SO_4 and are unlikely to play a major role in the corrosion mechanism within the liquid film [35], which was later confirmed by Shores, Fang and Rapp [53,54].

Fig. 9a shows the chemical analysis (by EDX) of the $Ti_{0.52}Al_{0.48}N$ coating surface that has been corroded with salt-deposits for 15 h at 700 °C in a SO_x-rich atmosphere. With the salt-deposits removed after the corrosion experiment, distinct differences in the severity of the corrosive attack are visible. Ring-like imprints reveal areas where the salt had contact with coating surface, and where voids/pores prevented the salt from causing corrosion (highlighted by the dotted circles). As the salt deposits are prepared by placing a drop of saturated salt-solution onto the surface of the coating, the subsequent drying process traps air within the slowly drying salt-deposit, and consequently forms a porous matrix. By reviewing the EDX-maps, significant depletion of Ti, Al and N is featured at places where the salt stood in contact with the coating surface. Simultaneously, O- and S-enrichment occurs where Al, N and Ti have diffused outward.

Fig. 9b, on the other hand, shows EDX-maps of the underside of the salt-deposit, revealing that indeed, Al and Ti are absorbed by the salt-deposit. This suggests that Al and Ti first migrate to the coating surface, where they oxidize and form Al_2O_3 and TiO_2 scales according to type T oxidation. Thereafter, an oxide to sulphate transformation takes place, after which a low melting sulphate-eutectic develops and a fluxing mechanism between the developing scales and salt-deposit proceeds.

In order to substantiate this claim, structural analyses were conducted of the as-deposited Na_2SO_4-$MgSO_4$ salt, as well as the salt-retrieval from the $Ti_{0.52}Al_{0.48}N$ coating after 15 h corrosion time at 700 °C (Figs. 10a and 10b, respectively). In the as-deposited form, the mixture is comprised solely of an orthorhombic $Na_2SO_4/MgSO_4$ mixture. After 15 h of corrosion time at 700 °C in a SO_x-rich atmosphere, the salt composition transitions to a predominantly monoclinic $Na_6Mg(SO_4)_4$ and orthorhombic $Na_2Mg_3(SO_4)_4$ composition, with residual orthorhombic Na_2SO_4 and $MgSO_4$ grains. Furthermore, the presence of orthorhombic TiO_2 and monoclinic $NaAl(SO_4)_2$ could be confirmed, which provides further evidence for the dissolution of Al_2O_3 and TiO_2 by the Na_2SO_4-$MgSO_4$ melt.

3.7. Detailed morphological analysis of $Ti_{1-x}Al_xN$ under LTHC conditions

TEM analyses were conducted to further understand, to which degree the subsequent propagation mechanisms (accelerated oxidation) of the $Ti_{0.52}Al_{0.48}N$ and $Ti_{0.34}Al_{0.66}N$ coincide and/or differ from one another.

The propagation stage (accelerated oxidation) of the $Ti_{0.52}Al_{0.48}N$ and $Ti_{0.34}Al_{0.66}N$ coating is presented throughout Figs. 11–13. Fig. 11a shows a bright field TEM cross-section image of the salt-loaded $Ti_{0.52}Al_{0.48}N$ after 15 h at 700 °C. In order to provide better contrast between individual coating structures, especially corroded areas near the surface, STEM imaging was performed at the area highlighted by the dotted box and shown in Fig. 11b. There, three distinctly different

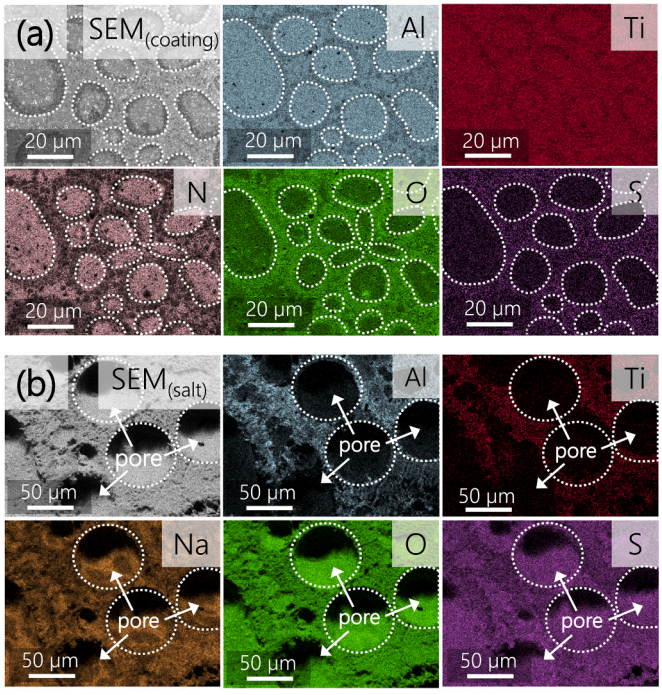

Fig. 9. EDX mapping showing (a) a top-view of the $Ti_{0.52}Al_{0.48}N$ coating surface after 15 h of corrosion time after the salt deposit removed, and (b) the underside of the respective salt-deposit extracted from the coating side shown in (a).

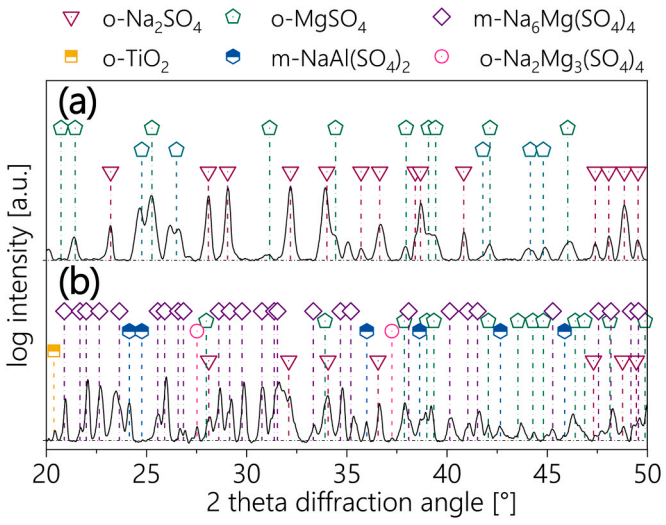

Fig. 10. X-ray diffractograms of (a) as-deposited 80/20 mol.% $Na_2SO_4/MgSO_4$ salt-mixture, and (b) salt-retrieval from the surface of a $Ti_{0.52}Al_{0.48}N$ coated Nimonic c-263 alloy after 15 h of annealing time in SO_x-rich atmosphere at 700 °C. Reference patterns were taken from ref. [55–60].

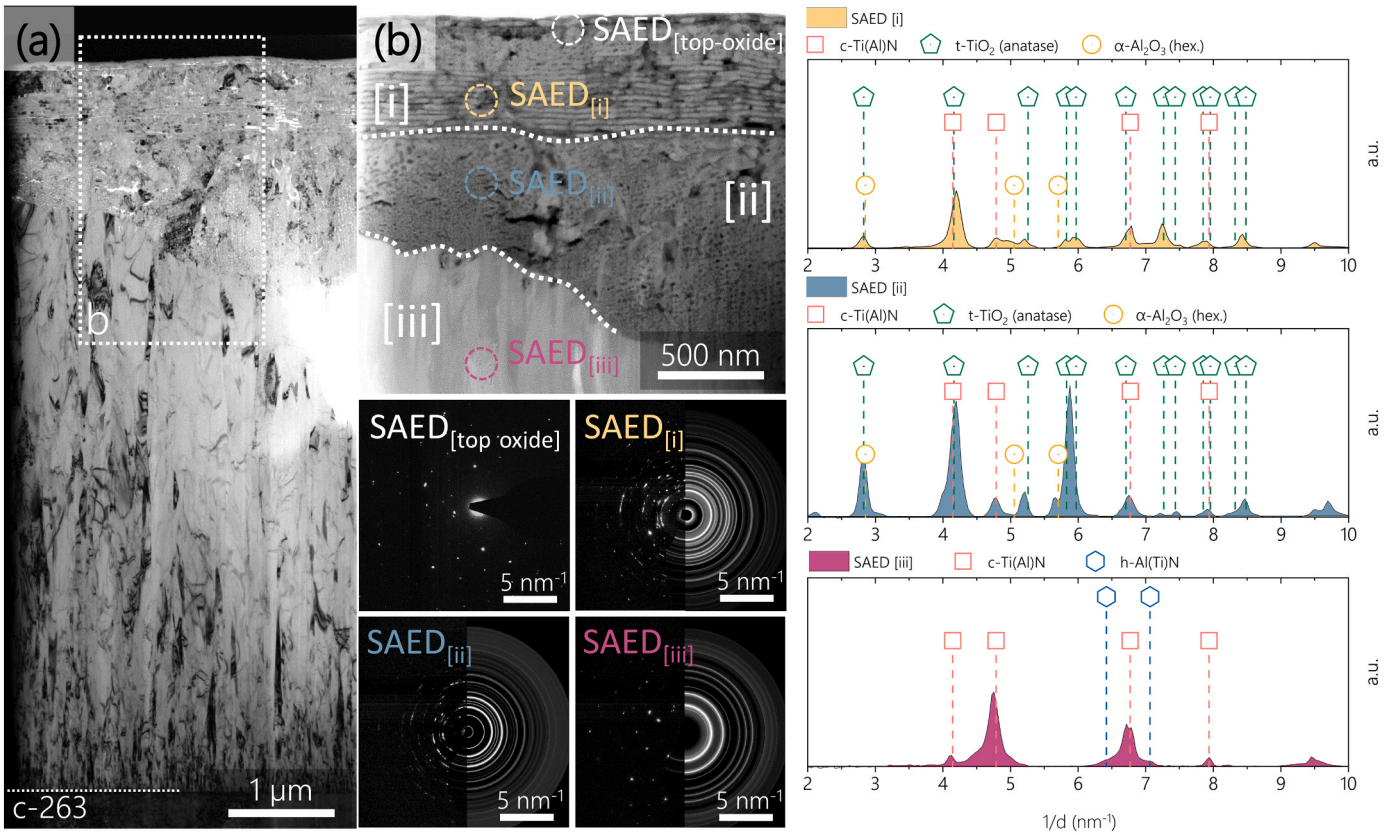

Fig. 11. TEM investigation featuring the propagation stage of the $Ti_{0.52}Al_{0.48}N$ coating after 15 h at 700 °C. (a) features a bright field TEM cross-section of the entire coating structure. (b) shows a STEM images of a selected surface near region (marked by the dotted box), highlighting the formation of three distinctly different coating microstructures (zone i,ii and iii). Lastly, SAEDs were obtained from each zone, whose integrated intensity plots are shown below.

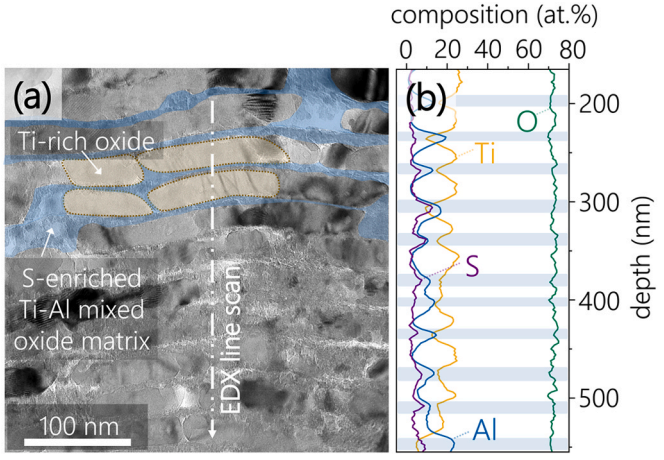

Fig. 12. TEM investigation of the highly lamellar coating structure (zone i), featuring the propagation stage of the $Ti_{0.52}Al_{0.48}N$ coating after 15 h at 700 °C: (a) bright-field image, featuring sequential Ti-rich crystalline domains, suspended in a disrupted S-enriched Ti-Al mixed oxide matrix. (b) provides the respective EDX line scan profiles.

coating morphologies are observed (labeled i, ii and iii). Starting from the top, a finely layered structure can be seen with distinct pore formations in between each layer (zone i). Underneath, a less ordered structure is featured with a more globular morphology and significant pore distribution (zone ii). Lastly, at the very bottom, the pristine coating morphology can be seen with its typical columnar structure (zone iii). In order to gain insight about the crystal structure of each distinct zone, SAEDs were collected. The location of each performed SAED is indicated in Fig. 11b and labeled according to the zones they were taken from ($SAED_{[i]}$, $SAED_{[ii]}$ and $SAED_{[iii]}$, pertain to the layered structure, globular feature, and pristine coating morphology, respectively, while the $SAED_{[top\ oxide]}$ refers to the oxide positioned at the surface). Starting from the top, the $SAED_{[top\ oxide]}$ renders single crystalline domains, as evident from the spot-pattern. Indexing of the pattern renders a trigonal crystal structure of the α-Al_2O_3 with the space group $R\bar{3}c$. $SAED_{[i]}$ and $SAED_{[ii]}$, on the other hand, exhibit smeared diffraction pattern, inferring a more distorted nanocrystalline structure. By integrating the SAED ring-patterns and plotting them over the reciprocal of the lattice-spacing, intensity plots with broadened but defined peaks are generated. The intensity plot obtained from zone i (layered structure, $SAED_{[i]}$) predominantly features TiO_2-reflexes, with minor diffraction intensity pertaining to α-Al_2O_3 and the c-Ti(Al)N crystal structure. Similarly, the intensity plot from zone ii exhibits the same constituents (TiO_2, α-Al_2O_3 and c-Ti(Al)N), however with different intensity distribution. Finally, the diffraction pattern from $SAED_{[iii]}$ provides spot like diffraction spots, whose integration render diffraction vectors that match the c-Ti(Al)N crystal structure with minor indication of the w-AlN phase.

By taking a closer look at zone ii (layered features) the presence of highly ordered TiO_2 is further validated. Fig. 12 shows a HR-TEM image from zone ii (Fig. 12a) together with an EDX-line scan (Fig. 12b). Quite evident are the formations of rod-like TiO_2-domains that are arranged periodically in a mesh composed of Ti, S, Al and O. While the individual TiO_2-domains measure around 100 × 30 nm in size, the mesh appears mostly amorphous with nanocrystalline grains suspended within.

Fig. 13 shows the corroded state of the $Ti_{0.34}Al_{0.66}N$ after 15 h at 700 °C, where four distinctly different coating morphologies can be observed (labeled i, ii, iii, and iv). Here too, the SAEDs provide insight

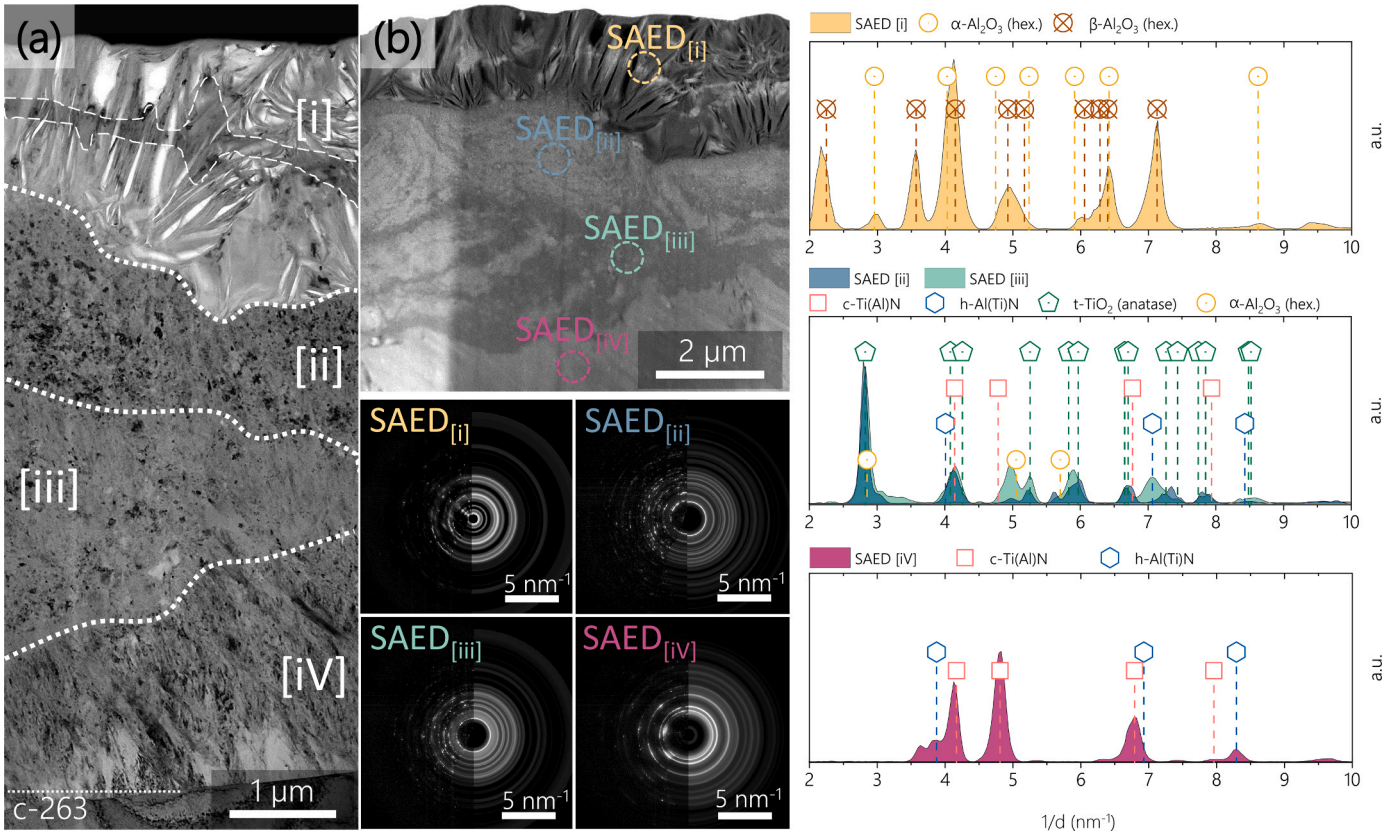

Fig. 13. TEM investigation featuring the propagation stage of the $Ti_{0.34}Al_{0.66}N$ coating after 15 h at 700 °C. (a) features a bright field TEM cross-section of the entire coating structure. (b) shows a STEM images of the face near region, highlighting the formation of four distinctly different coating microstructures (zone i, ii, iii, and iv). Lastly, SAEDs were obtained from each zone, whose integrated intensity plots are shown below.

about the crystal structure from each zone. Integration of the $SAED_{[i]}$ indicates diffraction vectors that match a mixed α-Al_2O_3 and β-Al_2O_3 oxide. While the α-configuration resembles the most common and thermodynamically stable form of Al_2O_3, the β-configuration represents a metastable structure, which forms together with sodium aluminate ($NaAl_{11}O_{17}$). The presence of both α- and β-crystal structures makes sense and validates the interaction between the Na_2SO_4 deposit and the forming Al-oxide scales.

Underneath, two globular morphologies can be seen (zone II and III). According to the respective $SAED_{[ii]}$ and $SAED_{[iii]}$, both zones feature a mixture of α-Al_2O_3, anatase-TiO_2 and residual c-Ti(Al)N. Unlike zone ii, zone iii ($SAED_{[iii]}$) features more pronounced α-Al_2O_3 reflexes, as well as peaks of the w-Al(Ti)N crystal structure.

Lastly, the $SAED_{[iv]}$ features diffraction vectors that fit the lattice spacing of the pristine as-deposited metastable c-Ti(Al)N crystal structure with indications of some indication of the w-Al(Ti)N phase.

4. Discussion

4.1. LTHC mechanism for $Ti_{1-x}Al_xN$ coatings

The LTHC mechanism for cathodic arc evaporated $Ti_{1-x}Al_xN$ coatings at 700 °C with a mixed Na_2SO_4-$MgSO_4$ salt-deposit is summarized schematically in Fig. 14.

4.1.1. Incubation stage

The LTHC mechanism begins with the incubation stage and the formation of a passive oxide scale. For protective coatings, particularly nitride-based coating such as $Ti_{1-x}Al_xN$, this entails a nitride to oxide transformation. The porous structure of the salt deposit facilitates eased permeation and subsequent diffusion of the oxidizing atmosphere to the coating surface, where both $Ti_{1-x}Al_xN$ coating variants developed a layered oxide scale (see Fig. 14a-b). According to the control group of this study, the scale formation for both, $Ti_{0.52}Al_{0.48}N$ and $Ti_{0.34}Al_{0.66}N$ coatings follow a type-T oxidation mechanism, where an Al-rich oxide forms on top, followed by a Ti-rich oxide underneath.

4.1.2. Initiation stage

The initiation stage comprises a sequence of changes in the materials environment that establishes the conditions where accelerated oxidation/degradation occurs. This is probably the most crucial step in the LTHC mechanism, as it roughly determines the longevity of protective coating. For LTHC, the initiations stage entails the formation of low-melting eutectics between the rigid salt-deposit and metal oxide surface. The formation of a liquid interface then allows for changes in the melt-basicity, and local depassivation of the oxide scale and/or nitride coating. For the establishment of a low-melting eutectic (liquid salt film) between the salt-deposit and the oxidized coating surface, sulphation of the oxide must occur. At sufficiently high pSO_3 in the atmosphere, the oxide-to-sulphate transition proceeds quite readily, but at low pSO_3, as is the case for this study, no sulphation of the coatings' top-oxides was observed (proven by control group, Fig. 5). Instead, SO_3 from the atmosphere permeates into the salt-deposit, where it accumulates, raises the local pSO_3 to a critical value (Fig. 14c-d) and initiates sulphation of the underlying oxide (Figs. 14e and 14e-*i*). As the formation of $Al_2(SO_4)_3$ progresses, a low melting eutectic $Al_2(SO_4)_3$-Na_2SO_4 mixture develops (Fig. 14f) and by extension transitions into a liquid salt interface (Fig. 14g). Within the liquid salt film, dissociation of Na_2SO_4 into its basic (Na_2O, O^{2-}) and acidic (SO_3) constituents (acid-base equilibrium $SO_4^{2-} \leftarrow\rightarrow O^{2-}+SO_3$) proceeds. Acidic and basic fluxing mechanisms are now possible, depending on the local basicity (activity of O^{2-} vs $S_2O_7^{2-}$). At the liquid-gas interface, SO_3 further acidifies the melt in the form of

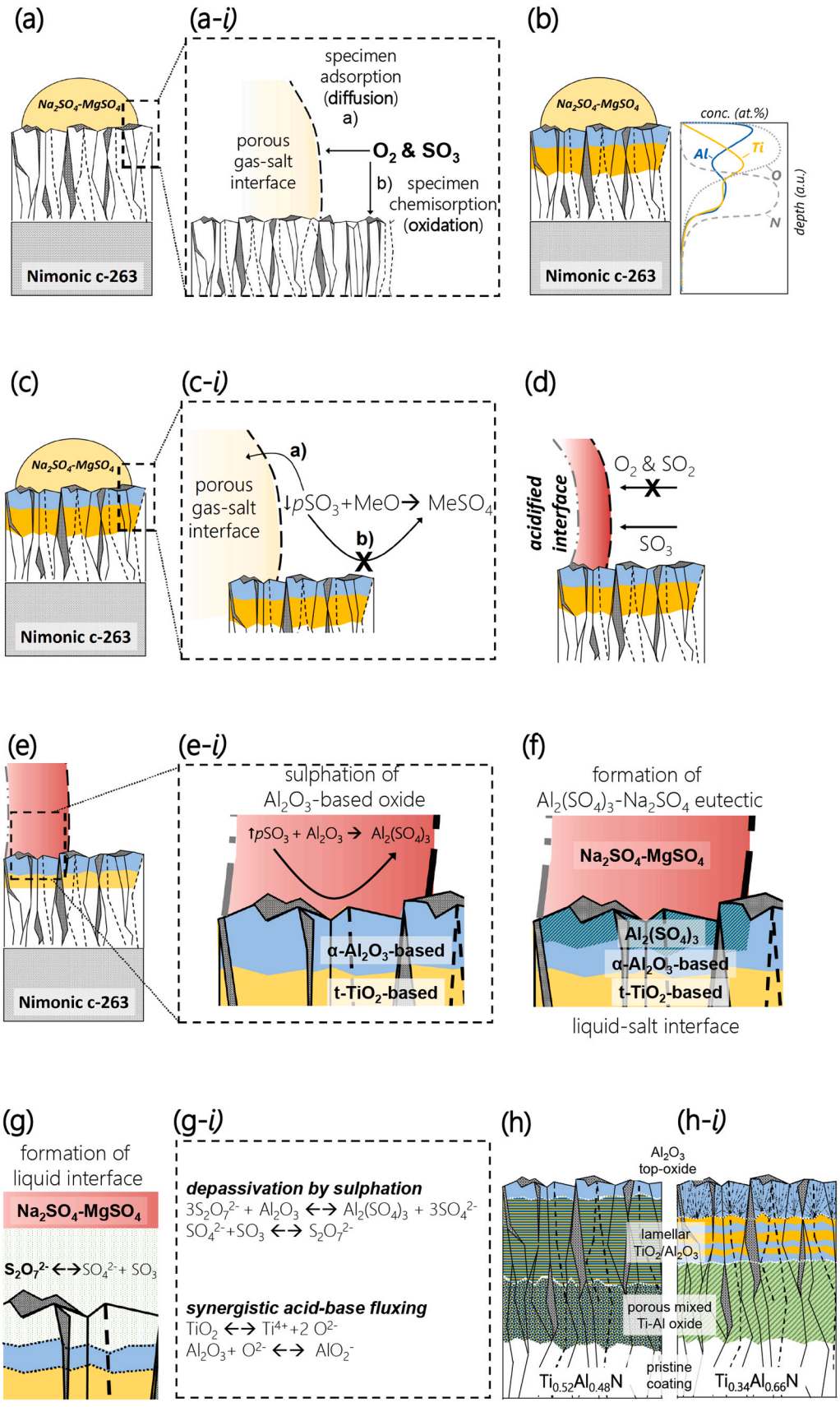

Fig. 14. Salt induced LTHC mechanism of cae-$Ti_{1-x}Al_xN$ coatings annealed at 700 °C in a SO_x-rich atmosphere.

$S_2O_7^{2-}$, which has been shown to be the major ionic carrier between the gas-salt-interface and the sample surface. Accordingly, dissolution of SO_3 in the form of $S_2O_7^{2-}$ produces additional acidic character, which further promotes the acidic fluxing of the Al-rich top oxide. This so-called gas-phase induced acidification of the salt-deposit is thereby a critical link in the LTHC mechanism and plays a crucial role in the initial depassivation of the oxide scale (Fig. 14g-*i*). Due to the relatively high stability of Al_2O_3 in acidic melts, its breakdown and acidic fluxing is proceeds quite slowly. This explains the different durations of the initiation stages, observed for both $Ti_{1-x}Al_xN$ coatings. Hence, a thicker Al_2O_3 top oxide contributes to a longer initiation stage ($Ti_{0.34}Al_{0.66}N$), whereas thinner Al_2O_3 scales provide less initial protection ($Ti_{0.52}Al_{0.48}N$).

4.1.3. Propagation stage

Once the Al_2O_3 top-oxide has been breached, a synergistic fluxing mechanism is proposed, where cooperative co-dissolution of TiO_2 and Al_2O_3 occurs. If the salt-melt basicity falls between the dissolution minima of two oxides (e.g. Al_2O_3 and TiO_2) then the more basic oxide (TiO_2 = more stable under basic conditions) undergoes acidic fluxing, whilst releasing oxide (O^{2-}) ions into the melt. The local increase in O^{2-} (increased basicity) then induces basic dissolution of the more acidic oxide (Al_2O_3 = more stable under acidic conditions) and in turn stimulates the acidic dissolution (Fig. 14g-*i*). In other words, when two oxides support the dissolution of the other, a faster degradation of the protective scale is expected then if both oxides were present individually. When assessing the corrosion rates of the $Ti_{0.52}Al_{0.48}N$ and $Ti_{0.34}Al_{0.66}N$ coatings, a synergistic fluxing mechanism could explain the alternating layering of the Al-rich and Ti-rich oxide bands. The synergistic effect may also explain the highly frequent layering within the corrosion pit of the $Ti_{0.52}Al_{0.48}N$. If the Al:Ti ≈ 1, then the switching between acidic and basic fluxing may occur more frequently, whereas if the Al:Ti ‡ 1, then the changeover occurs in a more irregular manner (Fig. 14h and h-*i*).

5. Conclusion

The present work deals with the LTHC behavior of $Ti_{1-x}Al_xN$ coated c-263 alloy when treated with a $Na_2SO_4/MgSO_4$ salt mixture and isothermally annealed in a SO_x-rich atmosphere. A series of annealing experiments revealed that the LTHC mechanism for $Ti_{1-x}Al_xN$ coatings can be expressed in four distinct stages: incubation, initiation, propagation, and failure.

First, oxidation of the $Ti_{0.52}Al_{0.48}N$ and $Ti_{0.34}Al_{0.66}N$ coatings occurs, leading to the formation of a layered oxide scale that is composed of an Al-rich layer on top and a Ti-rich oxide layer underneath (incubation stage).

Thereafter, sulphation of the oxide scale proceeds due to the SO_x-rich atmosphere, followed by the formation of a low-melting eutectic $Al_2(SO_4)_3$-Na_2SO_4, providing the necessary liquid-salt interface for accelerated corrosion to commence (initiation stage).

The ensuing propagation stage for both $Ti_{1-x}Al_xN$ variants could best be described by a synergistic fluxing mechanism of the individual Al_2O_3-rich and TiO_2-rich oxide layers. Depending on the relative Al-contents of the $Ti_{1-x}Al_xN$ coatings, distinct differences in the development of the corrosion scales were observed. While low Al-containing $Ti_{0.52}Al_{0.48}N$ coatings featured a thin Al_2O_3 top-oxide, followed by a highly laminated structure of Al-rich and Ti-rich oxide domains, higher Al-containing $Ti_{0.34}Al_{0.66}N$ coatings exhibited a much thicker Al_2O_3 top-oxide with a more spread out layering of Al-rich and Ti-rich oxide bands. To explain these differences, the authors propose that a more frequent synergistic co-dissolution of individual oxide bands takes place when the coating composition on the metal sublattice approaches 1:1 (Ti:Al), while a more irregular and sluggish fluxing occurs when metal-sublattice compositions are further apart.

Synergistic corrosion phenomena, as presented here for the binary $Ti_{1-x}Al_xN$ system, pose a significant challenge for developing HC protective coatings. As future coating strategies and systems tend to increase in complexity, the authors would like to emphasize the profound effect that chemical composition and synergy between elements within a coating have on the corrosion behavior in HC settings.

CRediT authorship contribution statement

O. E. H. and H. R. conceived the research. O. E. H. conducted the coating depositions, as well as the hot corrosion tests. P. K. prepared the TEM lamellas, whereas T. W. conducted the TEM measurements. O. H. and P. P. supported the research by providing indispensable funding, while L. S. and S. K. assisted the research with their thematic expertise. H. R. also provided funding acquisition and oversaw the research as supervisor. Finally, all authors have contributed in revising and approving the final version of the manuscript.

Declaration of Competing Interest

The authors declare the following financial interests/personal relationships which may be considered as potential competing interests: Helmut Riedl reports financial support was provided by Christian Doppler Research Association.

Data availability

The data that support the findings of this study are available from the corresponding author upon reasonable request.

Acknowledgments

The financial support by the Austrian Federal Ministry for Digital and Economic Affairs, the National Foundation for Research, Technology and Development and the Christian Doppler Research Association is gratefully acknowledged (Christian Doppler Laboratory "Surface Engineering of high-performance Components"). We also thank for the financial support of Plansee SE, Plansee Composite Materials GmbH, and Oerlikon Balzers, Oerlikon Surface Solutions AG. In addition, we want to thank the X-ray center (XRC) of TU Wien for beam time as well as the electron microscopy center - USTEM TU Wien - for providing the TEM facilities. The authors would like to extend our gratitude to Dr. Eckhardt and VDM Metals International GmbH for their generosity and support throughout this study. Lastly, the authors acknowledge TU Wien library for financial support through its Open Access Funding Program.

Appendices

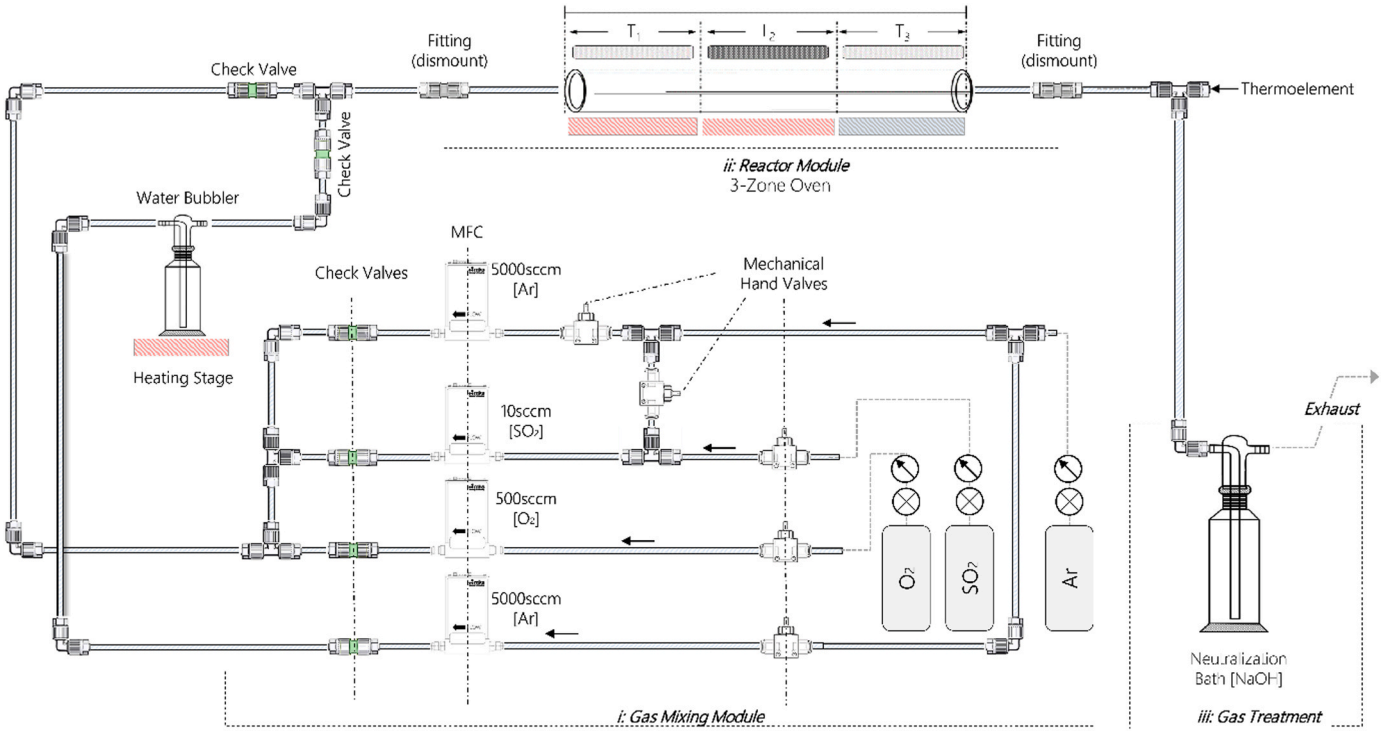

Fig. A1. Hot gas corrosion experimental set-up: (i) gas mixing system, (ii) quartz flow-reactor with a three-zone-gradient furnace, (iii) gas-treatment.

.

References

[1] H. Bisaria, P. Shandilya, Experimental investigation on wire electric discharge machining (WEDM) of Nimonic C-263 superalloy, Mater. Manuf. Process. 34 (2019) 83–92, https://doi.org/10.1080/10426914.2018.1532589.

[2] X. Zhang, Y. Chen, J. Hu, Recent advances in the development of aerospace materials, Prog. Aerosp. Sci. 97 (2018) 22–34, https://doi.org/10.1016/j.paerosci.2018.01.001.

[3] H.L. Cockings, B.J. Cockings, W. Harrison, M. Dowd, K.M. Perkins, M.T. Whittaker, G.J. Gibson, The effect of near-surface plastic deformation on the hot corrosion and high temperature corrosion-fatigue response of a nickel-based superalloy, J. Alloy. Compd. 832 (2020), 154889, https://doi.org/10.1016/j.jallcom.2020.154889.

[4] J.C. Zhao, V. Ravikumar, A.M. Beltran, Phase precipitation and phase stability in Nimonic 263, Metall. Mater. Trans. A Phys. Metall. Mater. Sci. 32 (2001) 1271–1282, https://doi.org/10.1007/s11661-001-0217-4.

[5] I. Gurrappa, Hot corrosion behavior of CM 247 LC alloy in Na2SO4 and NaCl environments, Oxid. Met. 51 (1999) 353–382, https://doi.org/10.1023/a:1018831025272.

[6] T.M. Pollock, S. Tin, Nickel-based superalloys for advanced turbine engines: chemistry, microstructure, and properties, J. Propuls. Power 22 (2006) 361–374, https://doi.org/10.2514/1.18239.

[7] Y. Zhao, Y. Zhang, Y. Zhang, Y. Luo, D. Tang, H. Liu, H. Fu, Deformation behavior and creep properties of Co-Al-W-based superalloys: a review, Prog. Nat. Sci. Mater. Int. 31 (2021) 641–648, https://doi.org/10.1016/j.pnsc.2021.09.009.

[8] N. Rao, Materials for gas turbines – an overview, Adv. Gas. Turbine Technol. (2011), https://doi.org/10.5772/20730.

[9] N.S. Patel, V. Pavlík, M. Boča, High-temperature corrosion behavior of superalloys in molten salts–a review, Crit. Rev. Solid State Mater. Sci. 42 (2017) 83–97, https://doi.org/10.1080/10408436.2016.1243090.

[10] N. Otsuka, R.A. Rapp, Hot corrosion of preoxidized Ni by a thin fused Na2 SO 4 film at 900°C, J. Electrochem. Soc. 137 (1990) 46–52, https://doi.org/10.1149/1.2086436.

[11] P. Song, M. Liu, X. Jiang, Y. Feng, J. Wu, G. Zhang, D. Wang, J. Dong, X.Q. Chen, L. Lou, Influence of alloying elements on hot corrosion resistance of nickel-based single crystal superalloys coated with Na2SO4 salt at 900 °C, Mater. Des. 197 (2021), 109197, https://doi.org/10.1016/j.matdes.2020.109197.

[12] V. Patarini, N.S. Bornstein, M.A. DeCrescente, Hot corrosion of gas turbine components, J. Eng. Gas. Turbines Power 101 (1979) 177–185, https://doi.org/10.1115/1.3446441.

[13] S. Hu, H. Finklea, X. Liu, A review on molten sulfate salts induced hot corrosion, J. Mater. Sci. Technol. 90 (2021) 243–254, https://doi.org/10.1016/j.jmst.2021.03.013.

[14] X. Ren, F. Wang, High-temperature oxidation and hot-corrosion behavior of a sputtered NiCrAlY coating with and without aluminizing, Surf. Coat. Technol. 201 (2006) 30–37, https://doi.org/10.1016/j.surfcoat.2005.10.042.

[15] G. Sreedhar, M.M. Alam, V.S. Raja, Hot corrosion behaviour of plasma sprayed YSZ/Al2O3 dispersed NiCrAlY coatings on Inconel-718 superalloy, Surf. Coat. Technol. 204 (2009) 291–299, https://doi.org/10.1016/j.surfcoat.2009.07.026.

[16] R. Jafari, E. Sadeghi, High-temperature corrosion performance of HVAF-sprayed NiCr, NiAl, and NiCrAlY coatings with alkali sulfate/chloride exposed to ambient air, Corros. Sci. 160 (2019), 108066, https://doi.org/10.1016/j.corsci.2019.06.021.

[17] H. Lin, W. Liang, Y. Jia, Q. Miao, R. Hu, Z. Ding, L. Yu, Effect of Al–Y gradient coating on hot corrosion resistance of γ-TiAl alloy at different temperatures, Appl. Surf. Sci. 487 (2019) 868–875, https://doi.org/10.1016/j.apsusc.2019.05.168.

[18] L.K. Wu, J.J. Wu, W.Y. Wu, H.J. Yan, M.Y. Jiang, F.H. Cao, Hot corrosion behavior of electrodeposited SiO2 coating on TiAl alloy, Corros. Sci. 174 (2020), 108827, https://doi.org/10.1016/j.corsci.2020.108827.

[19] R. Li, C. Cheng, J. Pu, NaCl-induced hot-corrosion behavior of TiAlN single-layer and TiAlN/Ti multilayer coatings at 500 °C, Mater. Today Commun. 33 (2022), 104421, https://doi.org/10.1016/j.mtcomm.2022.104421.

[20] M. Zhang, Y. Feng, Y. Wang, Y. Niu, L. Xin, Y. Li, J. Su, S. Zhu, F. Wang, Corrosion behaviors of nitride coatings on titanium alloy in NaCl-induced hot corrosion, Acta Metall. Sin. (Engl. Lett. 34 (2021) 1434–1446, https://doi.org/10.1007/s40195-021-01264-8.

[21] G. Biava, I.B. de Araujo Fernandes Siqueira, R.F. Vaz, G.B. de Souza, H.C. M. Jambo, A. Szogyenyi, A.G.M. Pukasiewicz, Evaluation of high temperature corrosion resistance of CrN, AlCrN, and TiAlN arc evaporation PVD coatings deposited on Waspaloy, Surf. Coat. Technol. 438 (2022), 128398, https://doi.org/10.1016/j.surfcoat.2022.128398.

[22] R.S. Bangari, S. Sahu, P.C. Yadav, Comparative evaluation of hot corrosion resistance of nanostructured AlCrN and TiAlN coatings on cobalt-based superalloys, J. Mater. Res. 33 (2018) 1023–1031, https://doi.org/10.1557/jmr.2018.53.

[23] Y. Qiao, X. Guo, X. Li, Hot corrosion behavior of silicide coating on an Nb-Ti-Si based ultrahigh temperature alloy, Corros. Sci. 91 (2015) 75–85, https://doi.org/10.1016/j.corsci.2014.10.053.

[24] J. He, X. Guo, Y. Qiao, F. Luo, A novel Zr-Y modified silicide coating on Nb-Si based alloys as protection against oxidation and hot corrosion, Corros. Sci. 177 (2020), 108948, https://doi.org/10.1016/j.corsci.2020.108948.
[25] H. Yu, Q. Fan, J. Li, D. Ma, J. Gong, C. Sun, Effect of Si addition to improve the performance of type II and type I hot corrosion resistance of aluminide coating, Corros. Sci. 212 (2023), 110937, https://doi.org/10.1016/j.corsci.2022.110937.
[26] Z. Tang, F. Wang, W. Wu, Effect of Al2O3 and enamel coatings on 900°C oxidation and hot corrosion behaviors of gamma-TiAl, Mater. Sci. Eng. A. 276 (2000) 70–75, https://doi.org/10.1016/S0921-5093(99)00513-4.
[27] H. Zhang, L. Yang, X. Zhang, Q. Wang, J. Wu, Z. Liu, C. Zeng, S. Zhu, Effect of enamel coating on the hot corrosion of 304 stainless steel beneath KCl–ZnCl2 deposits at 450 °C, J. Mater. Res. Technol. 23 (2023) 245–257, https://doi.org/10.1016/j.jmrt.2022.12.152.
[28] R.C. Brown, M.R. Anderson, C.E. Kolb, Aircr. Exhaust Sulfur Emiss. 23 (1996) 3603–3606.
[29] L.P. Belo, L.K. Elliott, R.J. Stanger, R. Spörl, K.V. Shah, J. Maier, T.F. Wall, High-temperature conversion of SO2 to SO3: homogeneous experiments and catalytic effect of fly ash from air and oxy-fuel firing, Energy Fuels 28 (2014) 7243–7251, https://doi.org/10.1021/ef5020346.
[30] S. Bose. High Temperature Coatings, 1st ed..,, Elsevier, 2007, https://doi.org/10.1016/B978-0-7506-8252-7.X5000-8.
[31] E. Yazhenskikh, T. Jantzen, D. Kobertz, K. Hack, M. Müller, Critical thermodynamic evaluation of the binary sub-systems of the core sulphate system Na2SO4–K2SO4–MgSO4–CaSO4, Calphad Comput. Coupling Phase Diagr. Thermochem. 72 (2021), https://doi.org/10.1016/j.calphad.2020.102234.
[32] J. Stringer, High-temperature corrosion of superalloys, Mater. Sci. Technol. 3 (1986) 482–493, https://doi.org/10.1080/02670836.1987.11782259.
[33] J.M. Alvarado-Orozco, J.E. Garcia-Herrera, B. Gleeson, F.S. Pettit, G.H. Meier, Reinterpretation of type II hot corrosion of Co-base alloys incorporating synergistic fluxing, Oxid. Met. 90 (2018) 527–553, https://doi.org/10.1007/s11085-018-9853-6.
[34] X. Zheng, R.A. Rapp, Electrochemical impedance of a platinum electrode in fused Na2 SO 4 melts in SO 2 – O 2 environments, J. Electrochem. Soc. 140 (1993) 2857–2862, https://doi.org/10.1149/1.2220922.
[35] K.L. Luthra, Low temperature hot corrosion of cobalt-base alloys" Part II, React. Mech. 13 (1982) 1853–1864.
[36] K.J. Meisner, E.J. Opila, Hot corrosion of shipboard gas turbine blades, Oxid. Met. 94 (2020) 301–322, https://doi.org/10.1007/s11085-020-09990-7.
[37] International Center of Diffraction Data, Powder diffraction file 04–001-3422, 2011.
[38] International Center of Diffraction Data, Powder diffractoin file 01–080-6097, 2013.
[39] International Center of Diffraction Data, Powder diffraction file 04–018-6856, 2022.
[40] L. Chavee, E. Serag, M. da Silva Pires, S. Lucas, E. Haye, A mechanistic approach of oxidation resistance, structural and mechanical behaviour of TiAlN coatings, Appl. Surf. Sci. 586 (2022), https://doi.org/10.1016/j.apsusc.2022.152851.
[41] P. Panjan, B. Navinšek, M. Čekada, A. Zalar, Oxidation behaviour of TiAlN coatings sputtered at low temperature, Vacuum 53 (1999) 127–131, https://doi.org/10.1016/S0042-207X(98)00407-2.
[42] G. Greczynski, L. Hultman, M. Odén, X-ray photoelectron spectroscopy studies of Ti1-xAlxN ($0 \leq x \leq 0.83$) high-temperature oxidation: the crucial role of Al concentration, Surf. Coat. Technol. 374 (2019) 923–934, https://doi.org/10.1016/j.surfcoat.2019.06.081.
[43] G. Greczynski, S. Mráz, L. Hultman, J.M. Schneider, Venting temperature determines surface chemistry of magnetron sputtered TiN films, Appl. Phys. Lett. 108 (2016), https://doi.org/10.1063/1.4940974.
[44] H.J. Maier, T. Niendorf, R. Bürgel, Handbuch Hochtemperatur- Werkstofftechnik, 6th ed., 2019.
[45] N. Burdett, W. Langdon, R.T. Squires, Rate coefficients for the reaction SO2+O2→SO3+O in the temperature range 900–1350 K, J. Inst. Energy (1984) 373.
[46] Y. Sarbassov, L. Duan, V. Manovic, E.J. Anthony, Sulfur trioxide formation/emissions in coal-fired air- and oxy-fuel combustion processes: a review, Greenh. Gases Sci. Technol. 8 (2018) 402–428, https://doi.org/10.1002/ghg.1767.
[47] International Center of Diffraction Data, Powder diffraction file 01–086-4330, 2020.
[48] International Center of Diffraction Data, Powder diffraction file 01–071-1169, 2020.
[49] International Center of Diffraction Data, Powder diffraction file 01–071-1684, 2022.
[50] International Center of Diffraction Data, Powder diffraction file 04–001-9278, 2011.
[51] International Center of Diffraction Data, Powder diffraction file 00–010-0414, 2003.
[52] F. Pettit, Hot corrosion of metals and alloys, Oxid. Met. 76 (2011) 1–21, https://doi.org/10.1007/s11085-011-9254-6.
[53] D.A. Shores, W.C. Fang, Transport of oxidant in molten Na2 SO 4 in O 2 – SO 2 – SO 3 environments, J. Electrochem. Soc. 128 (1981) 346–348, https://doi.org/10.1149/1.2127417.
[54] W.C. Fang, R.A. Rapp, Electrochemical reactions in a pure Na2 SO 4 melt, J. Electrochem. Soc. 130 (1983) 2335–2341, https://doi.org/10.1149/1.2119581.
[55] International Center of Diffraction Data, Powder diffraction file 00–027-0631, 1972.
[56] International Center of Diffraction Data, powder diffraction file 04–026-7237, 2019.
[57] International Center of Diffraction Data, Powder diffraction file 00–029-1240, 1978.
[58] International Center of Diffraction Data, Powder diffraction file 04–012-5048, 2011.
[59] International Center of Diffraction Data, Powder diffraction file 00–049-1433, 2003.
[60] International Center of Diffraction Data, Powder diffraction file 04–002-8228, 2005.